Article:

Wang, B., Wang, J. and Griffo, A. orcid.org/0000-0001-5642-2921 (2019) Stator turn fault modelling for a triple redundant 3x3-phase PMA SynRM. IEEE Transactions on Industrial Electronics, 66 (6). pp. 4220-4230. ISSN 0278-0046

https://doi.org/10.1109/TIE.2018.2866108

Stator Turn Fault Modelling for a Triple Redundant 3x3-phase PMA SynRM

Bo Wang, *Member IEEE*, Jiabin Wang, *Senior Member, IEEE*, Antonio Griffo, *Member IEEE*

***Abstract*—Accurate stator turn fault (STF) modelling technique is of paramount importance to assess the machine fault behavior and develop fault detection and mitigation strategies for a fault tolerant machine drive system. In this paper, a STF model is proposed for a triple redundant 3x3-phase permanent magnet assisted synchronous reluctance machine (PMA SynRM). The effect of turn fault current is represented by equivalent inputs to a general flux linkage model for each 3-phase set. Subsequently, the flux linkage of the fault turns is derived according to the coil location and slot position of the fault. The complete model is obtained by combining the flux linkage model with the governing voltage equations. The effectiveness and flexibility of the proposed model have been validated by extensive finite element (FE) simulations and experimental tests in various operation conditions. It is demonstrated that the model can predict the machine behavior with and without the mitigation action in the form of terminal short circuit (TSC).**

***Index Terms*—Fault tolerant, fault modelling, permanent magnet assisted synchronous reluctance machine, magneto-motive force, turn fault, fault location.**

I. Introduction

Stator turn fault, also commonly referred as inter-turn short-circuit fault, may lead to a catastrophic failure of electrical machine drives. It usually occurs in the first a few turns of a winding, due to excessive voltage stress resulting from PWM operation [1]. Electrical loading, thermal cycling, winding vibration and environmental contamination all contribute to the winding insulation degradation causing STF [2]. Since the faults only involve a few turns, large current is induced in the fault path which produces excessive heat and causes local hotspot. This further deteriorates the insulation and may lead to a complete failure [3].

Hence, machine behavior under STF should be investigated for assessing the fault impact and for development of fault detection and mitigation action [4]. A survey of STF modelling techniques has been presented in [5]. In [6], a transient model for an induction machine with STF was derived using reference frame transformation theory. STF in surface mounted permanent magnet machines was discussed in [7-11]. The inductance matrix of the faulty and healthy turns was extracted either by permeance network or FE simulation. An analytical approach was proposed in [12] to quantify the inductance and PM flux linkage. Particularly, it is shown that the slot leakage inductance has significant influence on the STF current.

An important fact is that, the machine winding distributions are no longer symmetrical in STF condition. In order to capture the changes in the winding distribution and resultant magneto-motive force (MMF), winding function [13, 14] has been used to calculate the inductance of each coil. The approach has been applied in a salient pole synchronous machine with coils in series and in parallel connections [15, 16]. In [4], a semi-analytical model for interior permanent magnet (IPM) machine with STF was developed. The flux linkage in fault condition is deduced using healthy *dq* flux linkage maps. A high fidelity STF model was developed in [17] based on the inverse of a 4 dimensional (4D) table extracted from FE simulation. However, it can only deal with the STF with fixed turns and fixed location. The investigations in [1, 3, 18] showed that both the slot location and coil location of the fault turns have significant impact on the fault current. They may also affect fault detection and mitigation actions. Therefore, an accurate and general model is essential to represent the machine with STF which may occur in different locations.

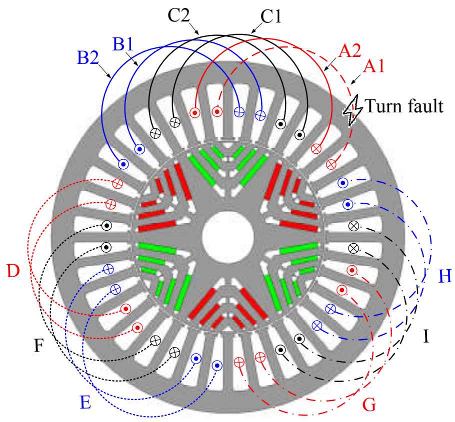

Fig. 1. PMA SynRM with segregated windings.

In [19], a triple redundant 3x3-phase PMA SynRM was proposed as shown in Fig. 1. The conventional overlapped windings are divided into three sets of separated 3-phase windings, resulting in physical and thermal isolation. The electrical isolation is achieved by using three standard 3-phase inverters to drive each set. This machine has been shown to be tolerant to the worst short-circuit fault – a single turn STF with application of TSC via inverter as the mitigation action [20]. After TSC, the resultant short circuit phase currents will essentially nullify the flux linkage in the fault turns and consequently, the STF current is reduced to a much lower value which is thermally sustainable for the

Manuscript received February 09, 2018; revised June 11, 2018; accepted August 06, 2018.

Bo Wang is with the School of Electrical Engineering, Southeast University, Nanjing, 210096, China (Email: bowang.ee@hotmail.com).

J. Wang and A. Griffo are with the Department of Electronic and Electrical Engineering, University of Sheffield, Sheffield S1 4DE, U.K (Email: j.b.wang@sheffield.ac.uk, a.griffo@sheffield.ac.uk).

machine. In addition, owing to the winding separation, other two 3-phase sets are isolated and can continue operation to generate torque.

However, although the different 3-phase sets are physically, thermally and electrically isolated, they are not magnetically isolated [20, 21]. The STF behavior is not only affected by the currents in the fault set, but also influenced by the currents in the other 3-phase sets. In addition, the STF behavior after TSC is further compounded by phase unbalance. The complex fault behavior of the fault tolerant drive system may be analyzed by FE and circuit based drive system co-simulation. This, however, is not practical even with today's computing power because of computationally demanding FE model and small time step (sub-micro second) required for drive system simulation, including PWM operation. Further since the factors such as the number of fault turns and the fault location in all possible coils and slots have significant influence on the machine and drive system under an STF, it is impossible to evaluate all the fault scenarios and assess the worst case by repeating computationally expensive FE-drive system co-simulation. Hence, a computationally efficient STF model which can represent the machine behavior in all possible scenarios will be indispensable for developing fault detection and mitigation algorithms for the machine drive over a wide operation range.

Thus, this paper aims to develop a STF model for the triple redundant 3x3-phase PMA SynRM. The model is mainly based on the general modelling technique described in [21] which can predict the machine behavior under healthy, one set open circuit, short circuit and unequal current operation conditions. The concept and approach are extended to incorporate the STF without generating new lookup tables. And the key influential factors, such as the number of fault turns and their position in the slot, the location of the faulted coil, and the currents in the faulty and healthy 3-phase sets, are all considered in the proposed turn fault model for generality. The rest of the paper is organized as follows. Section II introduces briefly the general fault modelling technique based on flux linkage map. Section III describes how a generic STF is represented in the flux linkage based model. The effectiveness of the proposed method is verified by extensive FE simulations in Section IV and experimental tests in section V. The findings are summarized in Section VI.

Table I
SPECIFICATIONS OF THE MACHINE

Specification	Symbol	Value
Base speed	n_b	4 000 rpm
Maximum speed	n_m	19 200 rpm
Rated power	P_r	33.5 kW
Rated current and gamma angle	I_{rated}	120 A (51°)
Nominal DC link voltage	V_{dc}	270 V
Turn number of each coil	N	8
Faulty turn number	N_f	1

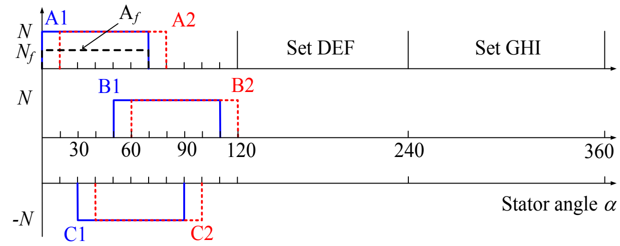

Fig. 2. Turn functions of the coils in set ABC.

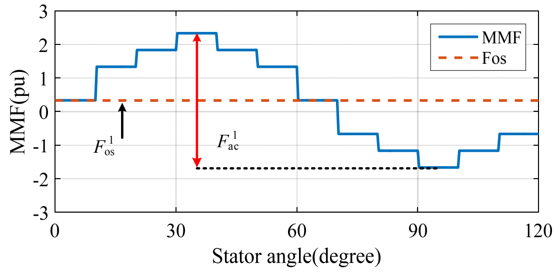

Fig. 3. MMF over set ABC region.

II. General Modelling Technique

The specifications of the machine under consideration are given in Table I. The three independent 3-phase windings of the machine are denoted as ABC, DEF and GHI. Each 3-phase winding set occupies 120 mechanical degrees with each phase consisting of two coils in series. By way of example, the turn functions of the coils in set ABC is plotted in Fig. 2 [14]. The distribution of the turn functions of a complete winding set is known as winding functions [22].

A general model has been proposed in [21] to represent the healthy, open circuit, terminal short circuit and unequal current operation conditions of the 3x3-phase machine. According to [21], the MMF over the whole airgap, which is calculated by multiplying the winding functions and phase currents, can be divided into three parts with each associated with a 3-phase set region. The typical MMF, F^1, over set ABC region is illustrated in Fig. 3. It consists of an AC component F_{ac}^1, and an offset component F_{os}^1, expressed as in (1).

$$\begin{aligned} F^1 &= F_{ac}^1 + F_{os}^1 \qquad\qquad 0° \le \alpha < 120° \\ F_{ac}^1 &= \textstyle\sum_{n=1,3,5\ldots} A_n \cos(3n\alpha + \delta_n) \\ F_{os}^1 &= \tfrac{2}{3}(i_A + i_B - i_C) - \tfrac{1}{3}(i_D + i_E - i_F) \\ &\quad - \tfrac{1}{3}(i_G + i_H - i_I) \end{aligned} \tag{1}$$

i_A, i_B … i_I are the phase currents. A_n and δ_n denote the amplitude and phase angle of the n^{th} MMF harmonic which are the functions of i_A, i_B, i_C only [23]. According to [21], the AC component F_{ac}^1 is purely determined by the currents in that set while the offset component F_{os}^1 is the combined effect of the currents in all three 3-phase sets. The phase currents i_A, i_B, i_C can be represented as i_{d1}, i_{q1} in dq axis system with respect to the rotor position θ. Therefore, the MMF over set ABC can be expressed in (2) as a function of $(\theta, i_{d1}, i_{q1}, F_{os}^1)$.

$$F^1 = f(\theta, i_{d1}, i_{q1}, F_{os}^1) \tag{2}$$

The MMFs over sets DEF and GHI can be expressed similarly as in (3), which also consist of an MMF AC component and an offset component. The variables are defined in the same manner as those for set ABC.

$$F^2 = F_{ac}^2 + F_{os}^2 = f(\theta, i_{d2}, i_{q2}, F_{os}^2)$$
$$F^3 = F_{ac}^3 + F_{os}^3 = f(\theta, i_{d3}, i_{q3}, F_{os}^3) \quad (3)$$

Thus, the MMF over each 3-phase set region can be expressed as a four-variable function, $f(\theta, i_d, i_q, F_{os})$, consisting of an MMF AC component and an offset component. (θ, i_d, i_q) determine the MMF AC components while F_{os} is the total offset component due to all three sets.

The MMF of each 3-phase set, denoted as $f(\theta, i_d, i_q, F_{os})$, determines the flux density in the airgap and hence induces flux linkages and torque in that region. As a result, the flux linkages and torque of one 3-phase set are functions of the four variables $(\theta,\ i_d,\ i_q, F_{os})$. They can be computed off-line by FE, and stored as 4D tables. Thus, the flux linkages and torque of one 3-phase set can be obtained by interpolating the 4D tables with the 4 input variables $(\theta, i_d, i_q, F_{os})$.

The block diagram of the proposed general modelling concept in [21] is illustrated in Fig. 4. The currents of each 3-phase set are fed into the MMF offset block to calculate the offset component F_{os} of each set according to (1). The *dq* axis currents together with rotor angle θ and the MMF offset component form the inputs $(\theta,\ i_{di},\ i_{qi},\ F_{os}^i, i = 1,2,3)$ to the 4D tables, and the resultant *dq0* axis flux linkages $(\varphi_{di}, \varphi_{qi}, \varphi_{0i})$ and torque of that 3-phase set T_i can be obtained from the look-up tables. The details of construction of the 4D tables through FE computation are described in [21]. The model captures the machine behavior in healthy, open circuit, short circuit and unequal current operation conditions. Its effectiveness has been verified in [21].

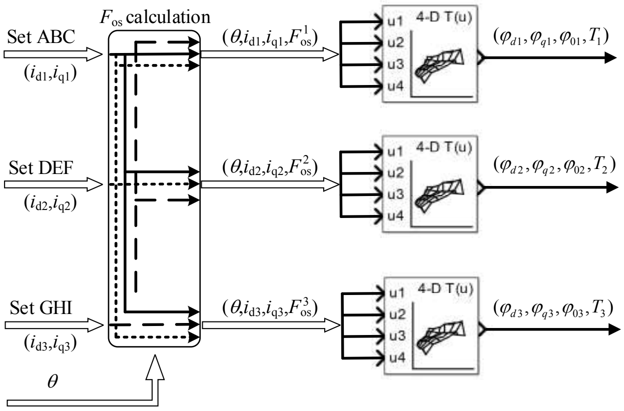

Fig. 4. General modelling diagram.

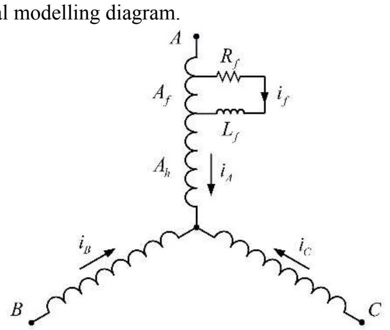

Fig. 5. Schematic circuit for set ABC with STF in phase A.

III. Turn Fault Modelling

The general fault modelling technique described in section II is extended to represent the machine behavior under stator turn fault.

Without loss of generality, the STF is assumed to occur in coil A1 of phase A of set ABC, as shown in Fig. 1. The schematic short circuit fault is illustrated in Fig. 5, where phase A has been divided into two parts, denoted as A_h for the healthy part, and A_f for the faulty part. N_f represents the number of short circuited turns and N is the turn number of a healthy coil. R_f and L_f represent the external resistance and inductance associated with the fault current path while i_f is the current in the fault path.

A. Equivalent Inputs for the General Model

According to the general modelling theory, the MMF of each 3-phase set can be described by $f(\theta, i_d, i_q, F_{os})$. In order to incorporate the STF into the model, the first step is to derive the equivalent inputs for the 4D tables considering the influence of fault current i_f for each 3-phase set.

In STF condition, significant fault current flows in the short circuit path and affects the MMF distribution. The influence of the short-circuit current on the MMF distribution can be accounted by MMF vectors based on the rotating field theory as described in [4]. In healthy condition, the fundamental MMF vectors produced by the two coils of phase A are shown in Fig. 6 and the combined effect can be expressed in the phasor form of (4).

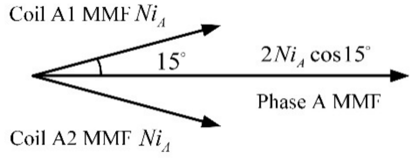

Fig. 6. MMF phasors of phase A.

$$MMF_A = Ni_A(e^{-j(p\theta+15°)} + e^{-j(p\theta-15°)})$$
$$= 2Ni_A \cos 15°\, e^{-j(p\theta)} \quad (4)$$

where p is the number of pole-pairs. Under STF conditions, the MMF vector of the fault current i_f within coil A1 is given in (5).

$$MMF_{Af} = -N_f i_f e^{-j(p\theta+15°)} \quad (5)$$

It should be noted that the MMF_{Af} is proportional to the number of short-circuited turns N_f. This MMF denoted by MMF_{Af} will affect the MMF AC component of the ABC winding set. Accordingly, Δi_{df}, Δi_{qf} given in (6) will be added to the original i_{d1}, i_{q1} to account this effect, and hence to obtain i_{df}, i_{qf} under the STF condition. It is worth noting that the fault current i_f does not contribute MMF AC components to the other two 3-phase sets.

$$\Delta i_{df} = -\frac{2}{3} * \frac{N_f}{2N \cos 15°} i_f \cos(p\theta + 15°)$$
$$\Delta i_{qf} = \frac{2}{3} * \frac{N_f}{2N \cos 15°} i_f \sin(p\theta + 15°) \quad (6)$$

In addition, the MMF offset component is altered. The extra offset component ΔF_{osf}^1 over set ABC due to i_f can be written in (7) according to the turn function of the fault turns as shown in Fig. 2.

$$\Delta F_{osf}^1 = -\frac{2}{3} * \frac{N_f}{2N} i_f \quad (7)$$

The new F_{osf}^1 is calculated by adding ΔF_{osf}^1 to the original F_{os}^1. The influence of i_f on the offset components of the other two 3-phase sets can be similarly derived and they are given in (8). F_{osf}^2 and F_{osf}^3 can be calculated by adding ΔF_{osf}^2, ΔF_{osf}^3 to F_{os}^2, F_{os}^3 respectively.

$$\Delta F_{osf}^2 = \Delta F_{osf}^3 = \frac{1}{3} * \frac{N_f}{2N} i_f \quad (8)$$

Finally, the modified four variables $(\theta, i_{df}, i_{qf}, F_{osf}^1)$ form the inputs to the 4D tables in Fig. 4 for the faulty set, while $(\theta, i_{d2}, i_{q2}, F_{osf}^2)$ and $(\theta, i_{d3}, i_{q3}, F_{osf}^3)$ are the inputs for DEF and GHI sets, respectively. Hence, the flux linkages and torque of each 3-phase set are obtained by interpolating the same 4D tables in [21], for accounting the influence of i_f and the number of fault turns N_f.

B. Flux Linkage of Fault Turns

The general model in Fig. 4 only provides the flux linkages in *dq0* frame for each 3-phase set. In order to predict the STF current, it is necessary to derive the flux linkage of the fault turns based on the flux linkages of the fault 3-phase set.

The flux linkage of the fault set can be divided into flux leakage and airgap flux linkages. The latter will be linked by both the healthy and fault turns [1]. Hence, the airgap flux linkages can be separated from the total flux linkages by (9), where φ_{mk}, (*k*= *d*, *q*, and *0*) denotes the airgap flux linkage in the k^{th} axis while L_l is the leakage inductance. φ_{m0} equals φ_0 since no zero sequence current exists in the 3-phase winding.

$$\begin{aligned} \varphi_{md} &= \varphi_{d1} - L_l i_{df} \\ \varphi_{mq} &= \varphi_{q1} - L_l i_{qf} \\ \varphi_{m0} &= \varphi_0 \end{aligned} \quad (9)$$

The airgap flux linkages are produced by the PM field and the armature reaction MMF. The PM flux linkage has a sinusoidal distribution in the airgap when the high order harmonics are ignored. As discussed above, the MMF in the airgap consists of an MMF AC component and an offset component. The resultant flux linkage is proportional to the MMF component. Thus, the flux linkage produced by the MMF AC component also has a sinusoidal distribution if the high order harmonics are ignored. However, this is not the case for the flux linkage produced by the offset component. All the airgap flux linkage components will be linked by the fault turns, however, they should be accounted separately due to different distributions.

First, the airgap flux linkage produced by the MMF offset component is considered. For example, the flux linkage of phase A due to the offset component F_{osf}^1 can be derived by (10) [22] where φ_{osA1} and φ_{osA2} denote the resultant airgap flux linkages for coils A1 and A2, respectively. n_{A1}, n_{A2} are the turn functions for coils A1 and A2 as shown in Fig. 2. r is the radius of the stator inner bore and l is the axial length of the stator stack. $g^{-1}(\alpha)$ is the inverse airgap function given in (11). The resultant flux linkages in phases B and C, φ_{osB} and φ_{osC}, can be derived similarly.

$$\begin{aligned} \varphi_{osA} &= \varphi_{osA1} + \varphi_{osA2} \\ &= \mu_0 r l \int g^{-1}(\alpha)\,(n_{A1} + n_{A2}) F_{osf}^1 d\alpha \end{aligned} \quad (10)$$

$$g^{-1}(\alpha) = a + b\cos(2\alpha + \alpha_0) \quad (11)$$

Fig. 7. Flux linkage distribution induced by the offset component.

Since the coils are full-pitched and F_{osf}^1 is constant over the region occupied by the ABC set, it can be shown that φ_{osA1} equals φ_{osA2}, and they have the same phase angle as φ_{osA}. Further, it can be deduced that φ_{osA} equals φ_{osB}. Due to the opposite polarity of the turn function for phase C compared to that of phases A and B, the offset flux linkage of phase C has an opposite polarity as shown in (12) and Fig. 7.

$$\varphi_{osA} = \varphi_{osB} = -\varphi_{osC} \quad (12)$$

Since the fault turns are located in coil A1, the flux linked by the fault turns is proportional to φ_{osA1} which is half of φ_{osA}. The flux linkages produced by the offset component, φ_{osA}, φ_{osB}, φ_{osC}, may be estimated from the 4D tables by (13) where dq^{-1} represents inverse dq transform. In the bracket, the first component denotes the flux linkages produced by the MMF AC and offset components together with the PMs while the second component denotes the flux linkages without the offset component. By subtracting the two components, the flux linkages produced by the offset component are obtained when the effect of magnetic saturation is neglected. Nonetheless, the saturation is insignificant in a turn fault case since the short circuit current tends to reduce the flux density in the fault region. Thus, the error caused by (13) would be relatively small as will be seen in the subsequent sections.

$$\begin{pmatrix} \varphi_{osA} \\ \varphi_{osB} \\ \varphi_{osC} \end{pmatrix} = dq^{-1} \begin{pmatrix} \varphi_d(\theta, i_{df}, i_{qf}, F_{osf}^1) - \varphi_d(\theta, i_{df}, i_{qf}, 0) \\ \varphi_q(\theta, i_{df}, i_{qf}, F_{osf}^1) - \varphi_q(\theta, i_{df}, i_{qf}, 0) \\ \varphi_0(\theta, i_{df}, i_{qf}, F_{osf}^1) - \varphi_0(\theta, i_{df}, i_{qf}, 0) \end{pmatrix} \quad (13)$$

The flux linkage of the fault turns due to the MMF offset component is proportional to the number of fault turns, *N_f*, and can be expressed in (14).

$$\varphi_{osAf} = \frac{N_f}{2N} \varphi_{osA} \quad (14)$$

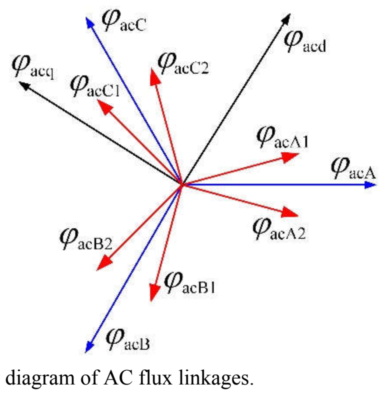

Fig. 8. Phasor diagram of AC flux linkages.

On the other hand, the flux linkages due to the PMs and MMF AC component have a sinusoidal distribution in the airgap and they are denoted as AC flux linkages (φ_{acA}, φ_{acB}, φ_{acC} for each phase). The phasor diagram of the AC flux linkages of the phases and coils are illustrated in Fig. 8. Therefore, the AC component of flux linkage of the fault turns is proportional to the AC flux linkage of coil A1, φ_{acA1}, where the fault occurs. However, φ_{acA1} differs from φ_{acA}

both in magnitude and phase angle. This explains why the different flux linkage components have to be dealt with separately.

Subtracting the total airgap flux linkages in (9) by the offset flux linkage components in (13) in the dq frame, the AC flux linkages of set ABC, φ_{acd}, φ_{acq}, φ_{ac0}, can be obtained in (15).

$$\begin{pmatrix}\varphi_{acd}\\ \varphi_{acq}\\ \varphi_{ac0}\end{pmatrix}=\begin{pmatrix}\varphi_{md}\\ \varphi_{mq}\\ \varphi_{m0}\end{pmatrix}-\begin{pmatrix}\varphi_{osd}\\ \varphi_{osq}\\ \varphi_{os0}\end{pmatrix} \tag{15}$$

The result can be projected to the fault turns in the direction of coil A1 axis given in (16) considering the coil location and the number of fault turns. The coil location of the fault turns is considered by the angle of coil A1 with respect to the d axis.

$$\begin{aligned}\varphi_{acAf}=&\frac{N_f}{2N\cos 15^\circ}(\varphi_{acd}\cos(p\theta+15^\circ)\\ &-\varphi_{acq}\sin(p\theta+15^\circ)+\varphi_{ac0})\end{aligned} \tag{16}$$

In addition, the slot leakage flux induced by the currents of the healthy and fault turns in coil A1 should be considered since it has noticeable impact on the fault current [1, 24]. The leakage flux of the fault turns φ_{lAf} is accounted by (17), where L_{lf} is the self-leakage inductance of the fault turns whereas M_{lf} is the mutual leakage inductance between the healthy turns and the fault turns in the same slot. It is worth noting that L_{lf} and M_{lf} are calculated according to the formulas in [1, 12] which are dependent on the slot position of the fault turns. Thus, the influence of the slot position of the fault turns is included.

$$\varphi_{lAf}=M_{lf}i_A+L_{lf}(i_A-i_f) \tag{17}$$

Finally, the total flux linkage of the fault turns can be obtained in (18) as a sum of (14), (16) and (17).

$$\varphi_{Af}=\varphi_{acAf}+\varphi_{osAf}+\varphi_{lAf} \tag{18}$$

C. Voltage Equations

Based on the derived flux linkages of the fault turns and fault set ABC, the voltage equations of the fault turns and the three 3-phase sets are written as follows. The resistance of the fault turns are proportional to the number of fault turns N_f.

$$\begin{aligned}&R_f i_f+L_f\frac{di_f}{dt}=\frac{N_f}{2N}R_s(i_A-i_f)+\frac{d\varphi_{Af}}{dt}\\ &u_{d1}=R_s i_{d1}+\frac{d\varphi_{d1}}{dt}-\omega\varphi_{q1}-\frac{N_f}{3N}R_s i_f\cos(p\theta)\\ &u_{q1}=R_s i_{q1}+\frac{d\varphi_{q1}}{dt}+\omega\varphi_{d1}+\frac{N_f}{3N}R_s i_f\sin(p\theta)\\ &u_{d2,3}=R_s i_{d2,3}+\frac{d\varphi_{d2,3}}{dt}-\omega\varphi_{q2,3}\\ &u_{q2,3}=R_s i_{q2,3}+\frac{d\varphi_{q2,3}}{dt}+\omega\varphi_{d2,3}\end{aligned} \tag{19}$$

The severity of the turn fault can represented by the external fault resistance R_f. In healthy case, the fault resistance is infinity leading to zero fault current. Whilst in fault case, the fault resistance decreases and becomes very small as the insulation breaks down. Hence, large fault current is induced as will be shown in the subsequent sections.

The voltage equations for the other two 3-phase sets remain unchanged as in healthy condition while the influence of the fault current has been considered by the MMF offset components in (8). Thus, the general model has been adapted for representing the machine behavior under the STF, taking into the account the coil location and slot position of the fault, and the number of fault turns.

The complete model is described by the flux linkages and torque LUTs of the three 3-phase windings shown in Fig. 4, the flux linkage of the faulted turns in (14)-(18) and the voltage equations in (19). They can be simulated using an algebraic-differential equation (ADE) solver, such as Simscape or Saber. The model can be used to study mitigation measures, for example, by application of terminal short-circuit when a turn fault is detected. It also allows for simulation of fault signatures and hence aids the development of fault detection algorithms.

IV. Simulation Validation

The developed STF model is examined by comparing the predictions by the model with FE results under different fault scenarios including faults occurred in different coils, with and without the mitigation action, namely application of TSC.

A. STF without Terminal Short Circuit

First, a single turn short circuit fault without TSC is evaluated. The STF occurred in coil A1 as discussed above. All 3-phase sets are excited by 120A phase currents with 51° gamma angle, i.e., the angle between the current vector and q-axis, at 4000rpm. This is the maximum torque per Ampere operating condition. The predicted turn fault current matches well with the FE result as shown in Fig. 9. It can be seen that the fault current is 9 times greater than the rate and this will cause significant distortion to the phase flux linkages as can be seen in Fig. 10, where the phase flux linkages predicted by the model with the equivalent inputs $(\theta, i_{df}, i_{qf}, F_{osf}^1)$ and by FE analysis are very close. The flux linkage of phase A where the fault is located is lower than those of phases B and C due to flux nullifying effect of the turn fault current. The resultant torque is also predicted by the proposed model with reasonable accuracy compared with the FE prediction as illustrated in Fig. 11. For the purpose of comparison, the healthy torque under the same operation condition is also shown in Fig. 11. As can be observed, the fault gives rise to a significant 2nd harmonic in the torque waveform under turn fault condition. The 2nd harmonic torque component is mainly caused by the turn fault current which breaks the symmetry of the multiple 3-phase operation.

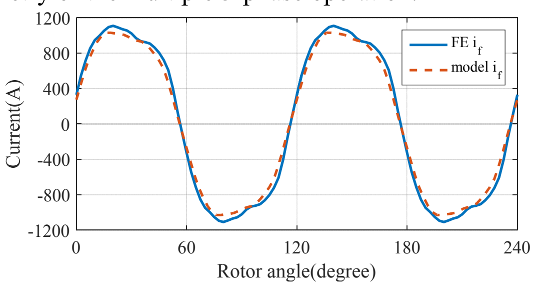

Fig. 9. Turn fault current with STF in coil A1 without TSC.

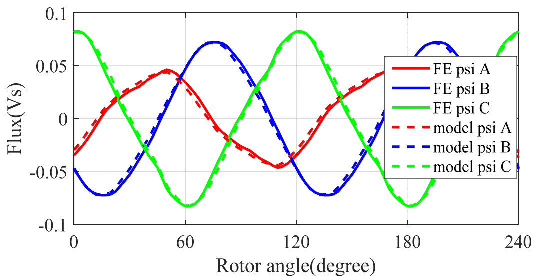

Fig. 10. Phase flux with STF in coil A1 without TSC.

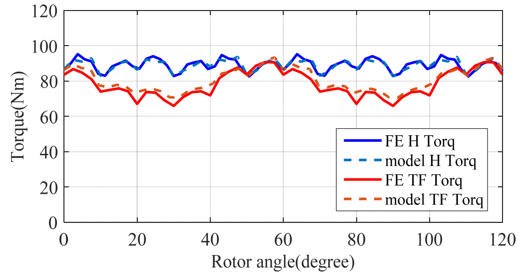

Fig. 11. Torque with STF in coil A1 without TSC.

Since the STF may occur in other coils, one turn short circuit in coil B2 is also examined under the same condition as previously stated. The resultant turn fault current is shown in Fig. 12. Again, the prediction matches well with the FE result. The phase flux linkages and torque are also accurately predicted and they are not given because similar behavior to those in Fig. 10 and Fig. 11 is observed. Thus, the model is capable of analyzing the STF behavior when the fault occurs in different coils.

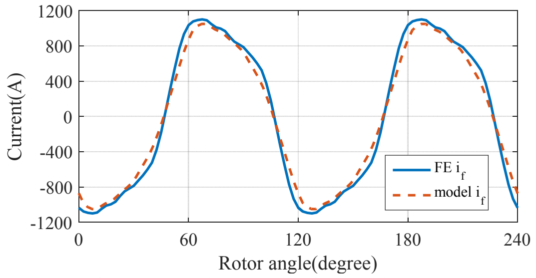

Fig. 12. Turn fault current with STF in coil B2 without TSC.

B. STF with Terminal Short Circuit

The excessive turn fault current would cause catastrophic damage to the machine and therefore mitigation action should be applied immediately. For the machine under consideration, the STF can be alleviated by applying TSC to the fault set. After the TSC, the voltages in (19) applied to the fault set become zero.

Initially, the single STF behavior in coil A1 with TSC is analyzed. The other two sets are still excited by the rated currents at 4000rpm with the same gamma angle. The resultant turn fault current and the phase currents predicted by the model and FE are compared in Fig. 13 and Fig. 14, respectively. Both the turn fault current and phase currents match well with the FE results. It is seen that the phase currents in the fault set is much lower than the rated. Consequently, although the rms current in the faulted turn is ~60% greater than the rated, the resultant overall heating effect of the faulty 3-phase set is indeed lower than the rated. Hence, the machine is capable of providing ~2/3 pu torque as shown in Fig. 15, where it is seen that the 2nd harmonic torque ripple is also much reduced after application of TSC.

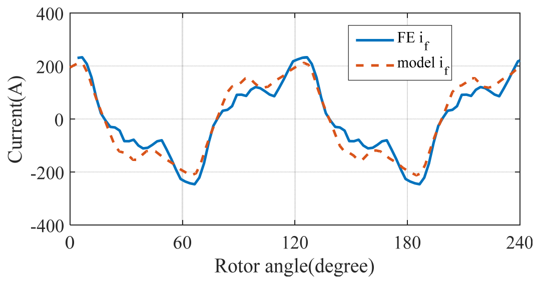

Fig. 13. Turn fault current with STF in coil A1 with TSC.

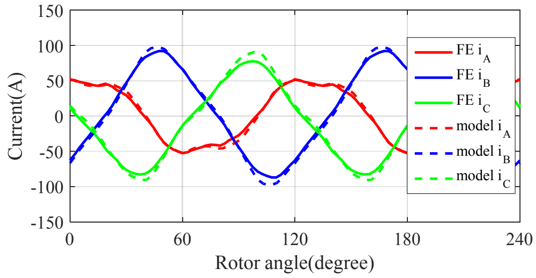

Fig. 14. Phase currents with STF in coil A1 with TSC.

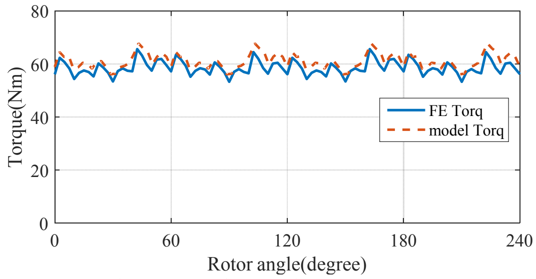

Fig. 15. Torque with STF in coil A1 with TSC.

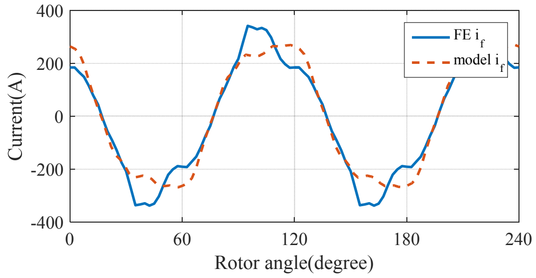

Fig. 16. Turn fault current with fault in coil B2 with TSC.

Similarly, one turn fault in coil B2 is evaluated under the same operation condition. The model and FE predicted turn fault current is reasonably close as shown in Fig. 16. Small error is noticed in the peak region which may be caused by ignoring the high order harmonics in the model derivations. And the turn fault current in coil B2 is higher than that of coil A1 which confirms the conclusion in [19].

It should be noted that although the model predictions are based on the FE lookup tables, the equivalent inputs for the flux linkage and torque LUTs and the flux linkage of the fault turns are derived based on a linear analysis and neglecting high order harmonics. They introduce prediction errors. Under TSC, the fault set phase currents are also predicted by the model. Hence, the errors in the phase current predictions also contribute to additional inaccuracy of the turn fault current. Nevertheless, the machine behavior with the rated current under saturation is well predicted albeit the errors in high order harmonics are evident.

V. Experimental Validation

The developed STF model has been validated by tests on a prototype 9-phase PMA SynRM whose specification is given in Table I. The machine is mounted on the dynamometer via the torque transducer as shown in Fig. 17. During the tests the dyno operates at a given speed while the machine is in torque control mode fed by a DSP-controlled 9-phase inverter, consisting of three 3-phase standard inverters. The same PI parameters of the DSP controller are used in the turn fault model to predict the fault behavior.

The STF test setup is illustrated in Fig. 18. A single turn fault has been specially implemented in coil A1 of set ABC. Thick cables have been connected to the fault turn to minimize the additional impedance. The leads are connected to the relay for fault emulation. The additional resistance and inductance of external cable leads is 1.2mΩ and 1μH while the resistance of the relay is 0.2mΩ. All these additional impedance has been considered in the model for predicting the STF behavior.

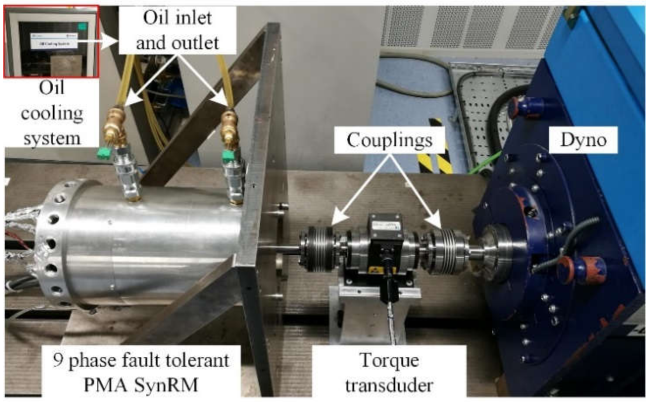

Fig. 17. The 9 phase PMA SynRM test rig.

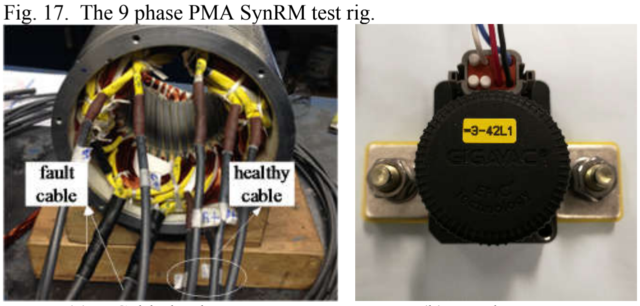

(a) Cable leads (b) Relay

Fig. 18. STF test setup.

A. STF without TSC

According to the analysis in section IV-A, the turn fault current without TSC is excessive at the rated operation point that may cause permanent damage. Thus, the STF in coil A1 is tested at 2000rpm while all three 3-phase sets are excited with 50A. The STF is triggered by closing the relay for 0.3s. The measured turn fault current matches well with the model prediction as shown in Fig. 19. Under this fault condition, the measured and predicted phase currents of the fault set are compared in Fig. 21 while the reference voltage from the DSP control and predicted voltages are compared Fig. 21. There are small mismatches in the reference and predicted voltages since the voltage applied to the windings are not exactly equal to the reference voltage due to inverter non-linearity. Similarly, the currents and voltages of the healthy DEF set are compared in Fig. 22 and Fig. 23 which also show good agreement. The currents and voltages in the healthy GHI set are similar and therefore not shown.

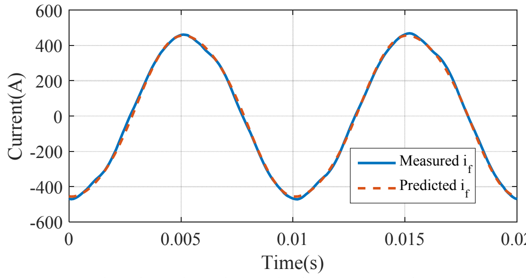

Fig. 19. Measured and predicted turn fault current with STF in coil A1.

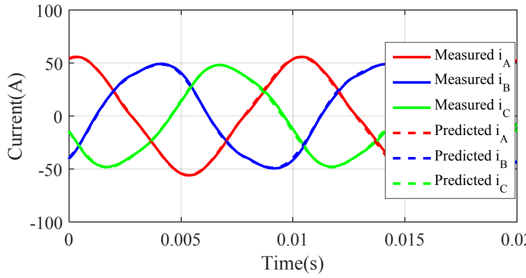

Fig. 20. Measured and predicted phase currents in faulty ABC set with STF in coil A1.

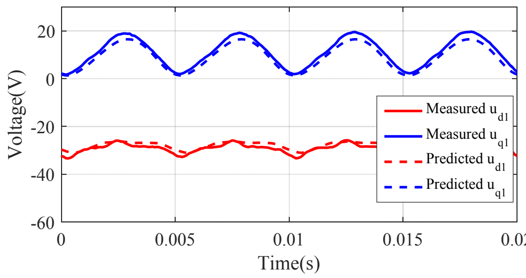

Fig. 21. Reference and predicted *dq* axis voltages of faulty ABC set with STF in coil A1.

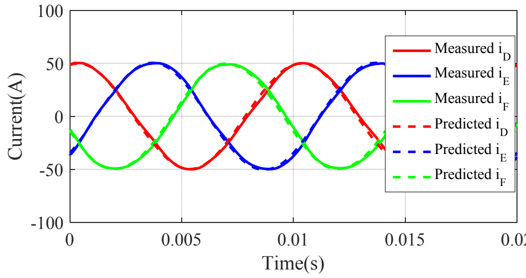

Fig. 22. Measured and predicted phase currents in healthy DEF set with STF in coil A1.

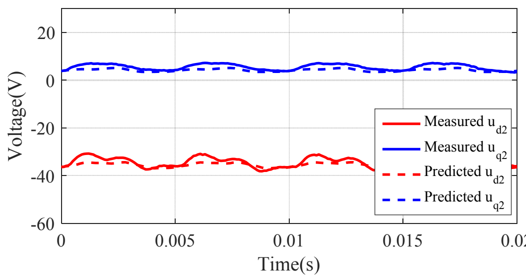

Fig. 23. Reference and predicted *dq* axis voltages of healthy DEF set with STF in coil A1.

The STF is also tested with different current excitation from 10A to 50A at 2000rpm. The measured and predicted rms fault currents are compared in Fig. 24. It is evident that predicted the fault current agrees well with the measurement under different operation conditions.

As shown in Fig. 1, coil A1 where the fault is emulated is the leading coil in the ABC 3-phase windings when the rotor rotates anti-clockwise. However, when the rotor rotates clockwise, it becomes the trailing coil, or equivalent to coil B2 when rotating anti-clockwise. Therefore, the fault current under the STF in coil B2 is measured by rotating the rotor in the reverse direction. The measured turn fault current with 50A in the healthy sets at 2000rpm is compared with the prediction in Fig. 26 while the measured and predicted rms variations of the fault current with the current excitation in the healthy sets from 10A to 50A at 2000rpm are compared in Fig. 27. Good agreements are seen in both cases.

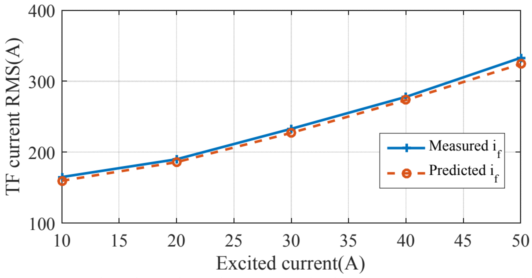

Fig. 24. Measured and predicted rms turn fault current variation with phase current under STF in coil A1.

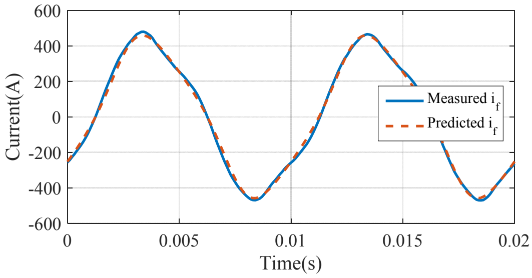

Fig. 25. Measured and predicted turn fault current with STF in coil B2.

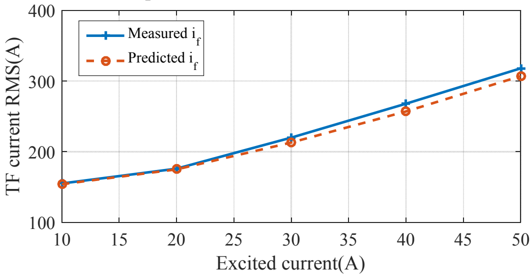

Fig. 26. Measured and predicted rms turn fault current variation with phase current under STF in coil B2.

B. *STF with TSC*

The STF behavior has also been tested with the application of mitigation action. After applying TSC on the fault set, the turn fault current is reduced to a much lower value. Thus, the STF can be tested at 4000rpm with 120A in healthy sets. Fig. 27 and Fig. 28 compare the measured and predicted turn fault current and phase currents in the faulted ABC set. The predictions match the measurements very well. It can be seen from Fig. 27 that while the measured and predicted fault currents are of similar waveforms to those in Fig. 13, their amplitudes are lower. This is because the additional impedance introduced in the fault emulation circuit is not considered in the simulation study in section IV-B. Meanwhile, the measured and predicted currents in the healthy DEF set is compared in Fig. 29 and the reference voltages and predicted voltages are compared in Fig. 30. Similar good agreements between the measurements and predictions are observed. The variations of the measured and predicted rms turn fault currents with phase currents in the healthy sets are shown in Fig. 31 where the maximum error below 10% is seen.

The STF currents in coil B2 with TSC under the same operation conditions are also measured and the results are compared with the predictions in Fig. 32 and Fig. 33. Again, similar good agreement between the measurements and predictions is evident. It is worth noting that the error in Fig. 33 is slightly higher than that of Fig. 31. This is because the error in predicting the fault set phase currents introduce additional error in prediction of the turn fault current using the proposed model.

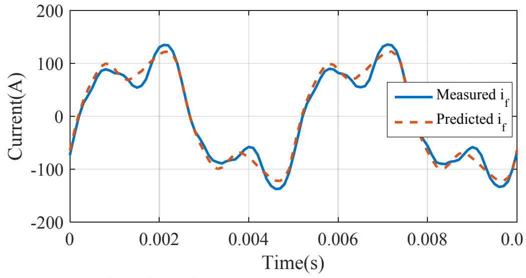

Fig. 27. Measured and predicted turn fault currents with STF in coil A1 when TSC is applied.

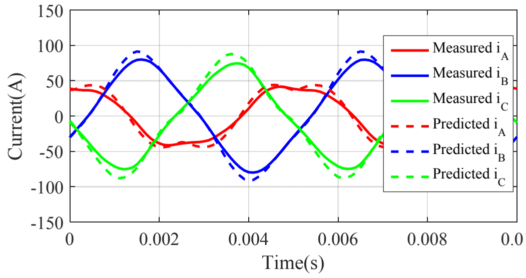

Fig. 28. Measured and predicted short circuit phase currents with STF in coil A1 when TSC is applied.

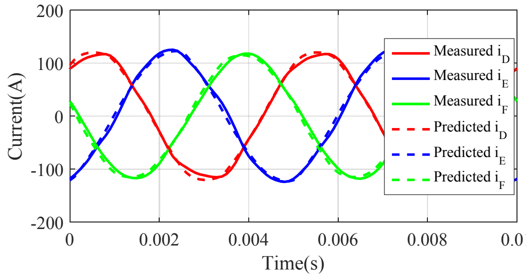

Fig. 29. Measured and predicted phase currents in healthy DEF set currents with STF in coil A1 when TSC is applied.

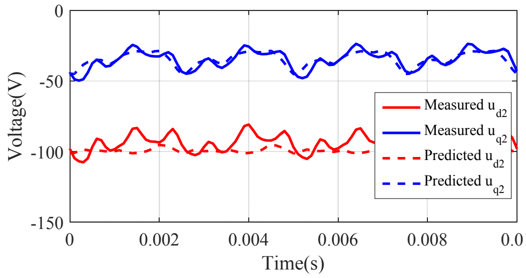

Fig. 30. Reference and predicted *dq* axis voltages in healthy DEF set with STF in coil A1 when TSC is applied.

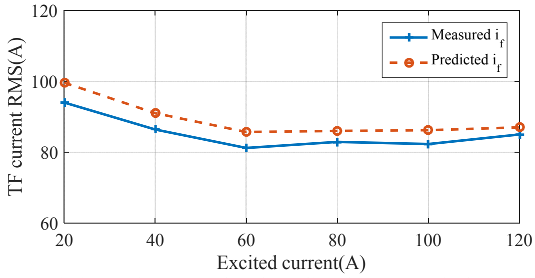

Fig. 31. Variations of measured and predicted rms turn fault current with phase current under STF in coil A1 when TSC is applied.

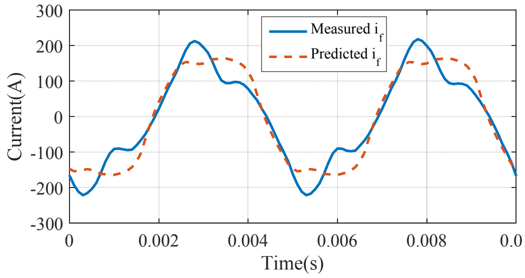

Fig. 32. Measured and predicted turn fault currents with STF in coil B2 when TSC is applied.

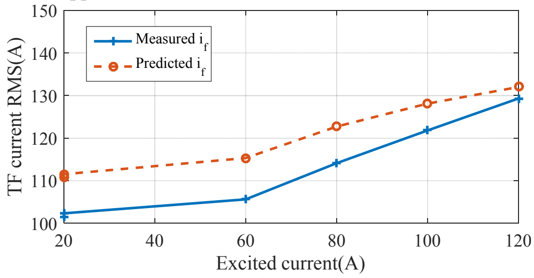

Fig. 33. Variations of measured and predicted rms turn fault current with phase current under STF in coil B2 when TSC is applied.

C. STF in Transient

The STF behavior has been also tested at 2000rpm with 50A phase current in transient mode. The measured turn fault current together with the phase currents are compared with the model predicted values in Fig. 34-Fig. 36. Initially, the machine is operating in healthy condition. The fault current is zero while the currents of sets ABC and DEF are symmetrical. A single turn fault is injected at 0.162s in coil B2. Consequently, large fault current is induced and its peak amplitude is about 460A as shown in Fig. 34. Some distortion is seen in the currents of the fault 3-phase set in Fig. 35 while the currents of the healthy set are still well controlled as shown in Fig. 36. It is seen that the measured fault current, the phase currents of the fault 3-phase set and the healthy 3-phase set all agree well with the model predictions. It confirms that the proposed model can capture the transient fault behavior with good accuracy. Therefore, the proposed model can be used to aid the development of fault detection techniques over the whole operation range and with different external fault resistance. It is not possible to test all fault scenarios as the fault current is destructive and may damage the machine. By employing the proposed model, the fault behavior and detection technique can be examined by simulation.

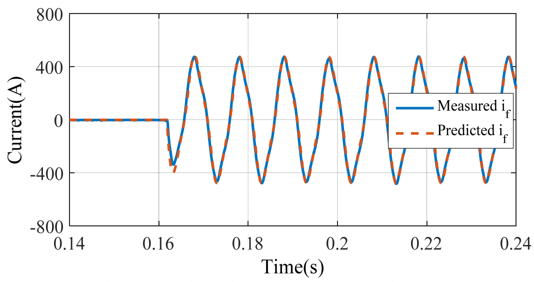

Fig. 34. Measured and predicted transient turn fault currents with STF in coil B2 at 2000rpm.

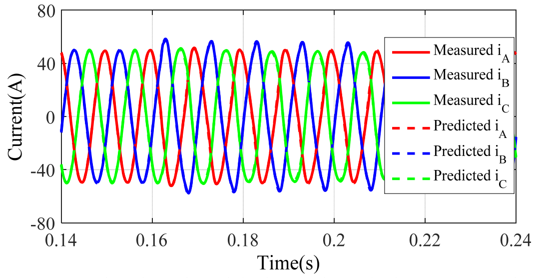

Fig. 35. Measured and predicted fault set phase fault currents with STF in coil B2 at 2000rpm.

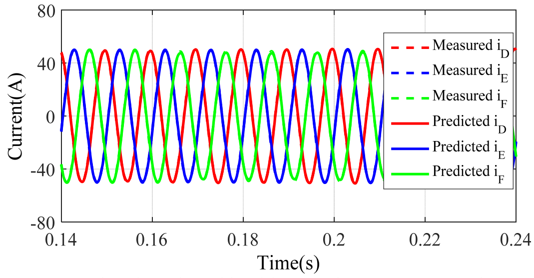

Fig. 36. Measured and predicted healthy set phase currents with STF in coil B2 at 2000rpm.

VI. Conclusion

In this paper, a STF model has been developed for a triple redundant 3-phase PMA SynRM accounting for the influence of fault location in different coils and slots, and the number of short-circuit turns. It is capable of predicting the machine STF behavior under various operating conditions with and without terminal short circuit. The developed fault model is computationally efficient, and it facilitates the development of fault detection and mitigation techniques. The accuracy of the model under various fault scenarios has been demonstrated by extensive FE simulations and experimental tests.

References

[1] Z. Sun, J. Wang, D. Howe, and G. Jewell, "Analytical Prediction of the Short-Circuit Current in Fault-Tolerant Permanent-Magnet Machines," *IEEE Transactions on Industrial Electronics,* vol. 55, pp. 4210-4217, 2008.

[2] A. H. Bonnett and G. C. Soukup, "Cause and analysis of stator and rotor failures in three-phase squirrel-cage induction motors," *IEEE Transactions on Industry Applications,* vol. 28, pp. 921-937, 1992.

[3] D. C. Patel and M. C. Chandorkar, "Modeling and Analysis of Stator Interturn Fault Location Effects on Induction Machines," *IEEE Transactions on Industrial Electronics,* vol. 61, pp. 4552-4564, 2014.

[4] B. Sen, J. Wang, and P. Lazari, "A detailed transient model of Interior Permanent Magnet motor accounting for saturation under stator turn fault," in *Energy Conversion Congress and Exposition (ECCE), 2013 IEEE*, 2013, pp. 3548-3555.

[5] A. Gandhi, T. Corrigan, and L. Parsa, "Recent Advances in Modeling and Online Detection of Stator Interturn Faults in Electrical Motors," *IEEE Transactions on Industrial Electronics,* vol. 58, pp. 1564-1575, 2011.

[6] R. M. Tallam, T. G. Habetler, and R. G. Harley, "Transient model for induction machines with stator winding turn faults," *IEEE Transactions on Industry Applications,* vol. 38, pp. 632-637, 2002.

[7] I. Jeong, B. J. Hyon, and K. Nam, "Dynamic Modeling and Control for SPMSMs With Internal Turn Short Fault," *IEEE Transactions on Power Electronics,* vol. 28, pp. 3495-3508, 2013.

[8] O. A. Mohammed, Z. Liu, S. Liu, and N. Y. Abed, "Internal Short Circuit Fault Diagnosis for PM Machines Using FE-Based Phase Variable Model and Wavelets Analysis," *IEEE Transactions on Magnetics,* vol. 43, pp. 1729-1732, 2007.

[9] B. Vaseghi, B. Nahid-mobarakh, N. Takorabet, and F. Meibody-Tabar, "Inductance Identification and Study of PM Motor With Winding Turn

Short Circuit Fault," *IEEE Transactions on Magnetics,* vol. 47, pp. 978-981, 2011.
[10] N. Leboeuf, T. Boileau, B. Nahid-Mobarakeh, N. Takorabet, F. Meibody-Tabar, and G. Clerc, "Inductance Calculations in Permanent-Magnet Motors Under Fault Conditions," *IEEE Transactions on Magnetics,* vol. 48, pp. 2605-2616, 2012.
[11] F. Wu, P. Zheng, and T. M. Jahns, "Analytical modeling of inter-turn short circuit for multiphase fault-tolerant PM machines with fractional-slot concentrated windings," in *Energy Conversion Congress and Exposition (ECCE), 2015 IEEE*, 2015, pp. 6970-6977.
[12] B. Sen and J. Wang, "Analytical modelling of stator turn fault in surface mounted permanent magnet machines," in *Energy Conversion Congress and Exposition (ECCE), 2013 IEEE*, 2013, pp. 4445-4452.
[13] K. Kyung-Tae, P. Jun-Kyu, H. Jin, and K. Byeong-Woo, "Comparison of the Fault Characteristics of IPM-Type and SPM-Type BLDC Motors Under Inter-Turn Fault Conditions Using Winding Function Theory," *IEEE Transactions on Industry Applications,* vol. 50, pp. 986-994, 2014.
[14] T. Kim, H. W. Lee, and S. Kwak, "The Internal Fault Analysis of Brushless DC Motors Based on the Winding Function Theory," *IEEE Transactions on Magnetics,* vol. 45, pp. 2090-2096, 2009.
[15] X. Tu, L. A. Dessaint, M. E. Kahel, and A. O. Barry, "A New Model of Synchronous Machine Internal Faults Based on Winding Distribution," *IEEE Transactions on Industrial Electronics,* vol. 53, pp. 1818-1828, 2006.
[16] X. Tu, L. A. Dessaint, N. Fallati, and B. D. Kelper, "Modeling and Real-Time Simulation of Internal Faults in Synchronous Generators With Parallel-Connected Windings," *IEEE Transactions on Industrial Electronics,* vol. 54, pp. 1400-1409, 2007.
[17] B. Sen, J. Wang, and P. Lazari, "A High-Fidelity Computationally Efficient Transient Model of Interior Permanent-Magnet Machine With Stator Turn Fault," *IEEE Transactions on Industrial Electronics,* vol. 63, pp. 773-783, 2016.
[18] P. Arumugam, "Design Optimization on Conductor Placement in the Slot of Permanent Magnet Machines to Restrict Turn-turn Short-Circuit Fault Current," *IEEE Transactions on Magnetics,* vol. 52, pp. 1-8, 2016.
[19] B. Wang, J. Wang, and A. Griffo, "A Fault Tolerant Machine Drive Based on Permanent Magnet Assisted Synchronous Reluctance Machine " in *Energy Conversion Congress and Exposition (ECCE), 2016 IEEE*, Milwaukee, WI, 2016, pp. 1-8.
[20] B. Wang, J. Wang, A. Griffo, and B. Sen, "Experimental Assessments of a Triple Redundant 9-Phase Fault Tolerant PMA SynRM Drive," *IEEE Transactions on Industrial Electronics,* early access, 2018.
[21] B. Wang, J. Wang, A. Griffo, and B. Sen, "A General Modelling Technique for a Triple Redundant 3x3-phase PMA SynRM," *IEEE Transactions on Industrial Electronics,* early access, 2018.
[22] J. Faiz and I. Tabatabaei, "Extension of winding function theory for nonuniform air gap in electric machinery," *IEEE Transactions on Magnetics,* vol. 38, pp. 3654-3657, 2002.
[23] X. Chen, J. Wang, V. I. Patel, and P. Lazari, "A Nine-Phase 18-Slot 14-Pole Interior Permanent Magnet Machine With Low Space Harmonics for Electric Vehicle Applications," *IEEE Transactions on Energy Conversion,* vol. 31, pp. 860-871, 2016.
[24] P. Arumugam, T. Hamiti, C. Brunson, and C. Gerada, "Analysis of Vertical Strip Wound Fault-Tolerant Permanent Magnet Synchronous Machines," *IEEE Transactions on Industrial Electronics,* vol. 61, pp. 1158-1168, 2014.

Bo Wang (M'17) received the B.Eng. and M.Sc. degrees in electrical engineering from Nanjing University of Aeronautics and Astronautics, Nanjing, China, in 2009 and 2012, respectively and the Ph.D. degree in Electronic and Electrical Engineering from the University of Sheffield, Sheffield, U.K., in 2018.

From 2012 to 2014, he served as a senior engineer in the Delta Electronics Co. Ltd. From 2017 to 2018, he was a research associate at the Department of Electronic and Electrical Engineering, University of Sheffield. Since 2018, he has joined the School of Electrical Engineering, Southeast University. His research interests include the permanent magnet machine drives, electric traction and fault tolerant systems.

Jiabin Wang (SM'03) received the B.Eng. and M.Eng. degrees from Jiangsu University, Zhengjiang, China, in 1982 and 1986, respectively, and the Ph.D. degree from the University of East London, London, U.K., in 1996, all in electrical and electronic engineering.

Currently, he is a Professor in Electrical Engineering at the University of Sheffield, Sheffield, U.K. From 1986 to 1991, he was with the Department of Electrical Engineering at Jiangsu University, where he was appointed a Lecturer in 1987 and an Associated Professor in 1990. He was a Postdoctoral Research Associate at the University of Sheffield, Sheffield, U.K., from 1996 to 1997, and a Senior Lecturer at the University of East London from 1998 to 2001. His research interests range from motion control and electromechanical energy conversion to electric drives for applications in automotive, renewable energy, household appliances and aerospace sectors.

He is a fellow of the IET and a senior member of IEEE.

Antonio Griffo (M'13) received the M.Sc. degree in electronic engineering and the Ph.D. degree in electrical engineering from the University of Napoli "Federico II," Naples, Italy, in 2003 and 2007, respectively. From 2007 to 2013, he was a Research Associate with the University of Sheffield, Sheffield, U.K., and the University of Bristol, Bristol, U.K. He is currently a Lecturer with the Department of Electronic and Electrical Engineering, University of Sheffield. His research interests include modeling, control and condition monitoring of electric power systems, power electronics converters, and electrical motor drives, for renewable energy, automotive and aerospace applications.